Multi-Regional CT Radiomics Fusion to Quantify Pathology-Derived Pollutant Burden in Lung Cancer

Yutong Li[1], Xiaoxi Pan[1], Abishek Balachandran[1], Carmen Behrens[1], Maria Esther Salvatierra[1], Luisa Maren Solis Soto[1], Chingyi Young[1], Yinyin Yuan[1(✉)], Chengyue Wu[1,2(✉)]

[1]The University of Texas MD Anderson Cancer Center, Houston, TX 77030, USA
[2]Oden Institute for Computational Engineering and Sciences, The University of Texas at Austin, Austin, TX 78712, USA
YYuan6@mdanderson.org, CWu19@mdanderson.org

Abstract. Anthracotic carbon pigment deposition reflects cumulative inhaled particulate exposure and is only visible in histopathology, which is however invasive, limiting scalability for screening and longitudinal monitoring. We developed a CT-based radiomics framework to non-invasively estimate pollutant burden using pathology-derived lung pollutant measure as reference. We extracted standardized radiomic features from six anatomical regions (tumor, whole lung, normal lung, and 5/10/15-mm peritumoral rings) and trained region-specific classifiers with nested cross-validation. Region-specific classifiers trained via cross-validated feature selection were integrated through weighted late-fusion. In an in-house cohort (n=145), multi-regional fusion achieved AUC=0.733 (95% CI: 0.644–0.812), outperforming single-region models (best AUC=0.664). Normal lung parenchyma contributed most strongly (weight=0.40), with texture heterogeneity features dominating. External evaluation on a subset of National Lung Screening Trial (NLST) (n=194) demonstrated maintained discriminative performance under domain shift (AUC=0.609, 95% CI: 0.513–0.702). Subgroup analyses suggested the model is not driven by smoking status, confirming pollution-specific signal capture. This framework provides a noninvasive, mechanism-anchored approach to quantify pollutant-associated phenotypes from routine chest CT.

Keywords: Lung Pollutant Burden, Chest CT, Machine Learning, Lung Adenocarcinoma

1 Introduction

Lung adenocarcinoma (LUAD) represents a major subtype of non-small cell lung cancer, with increasing incidence in never-smokers [1-3]. While environmental air pollution and inhaled particulate matter are recognized risk factors [4, 5], accurate individual level exposure assessment remains challenging, as clinical practice relies on self-report or geospatial proxies which are qualitative and inadequate for personalized risk stratification. Our prior work defined a Lung Pollutant Index (LPI) by automated pigment

quantification on routine pathology images. Such computational histopathology-based assessment offers a biological approach to quantify cumulative pollutant burden through anthracotic carbon pigment deposition in lung tissue, demonstrating the potential to robustly quantify individual pollution exposure. However, this measure is invasive and cannot be directly applied for population screening or longitudinal monitoring.

Complementarily, chest CT is non-invasive, ubiquitous in lung cancer management [6], and encodes rich phenotypic information beyond visible nodules. Radiomics have shown success in extracting high-dimensional features of tissue heterogeneity and structural patterns [7-9]. Moreover, prior CT radiomics studies in pollution-associated diseases such as COPD have reported measurable parenchymal phenotype difference [10-12], suggesting CT may reflect pollutant deposition.

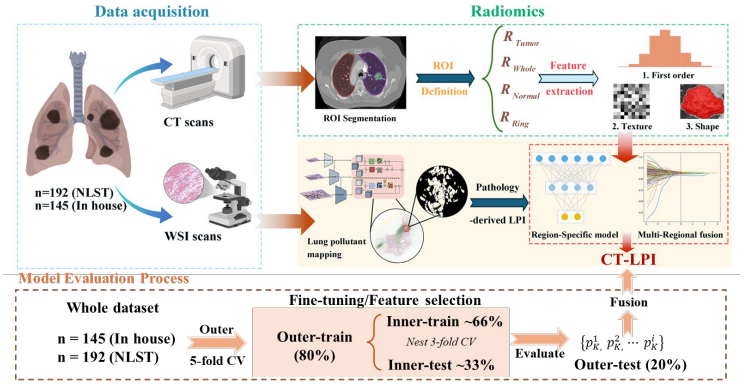

Fig. 1. CT-LPI framework for multi-regional fusion. Radiologist-provided lung and tumor segmentations define six ROIs (tumor, whole lung, normal lung, and 5/10/15-mm peritumoral rings), from which standardized PyRadiomics features [13] are extracted to train region-specific classifiers and integrate their outputs via late-fusion ensembles to predict LPI.

As shown in **Fig. 1**, we developed a framework to estimate CT-based pollutant burden, CT Lung Pollutant Index (CT-LPI), from preoperative chest CT using corresponding surgical pathology-derived LPI as reference in a retrospective LUAD cohort. Considering pollutant-related phenotypes may manifest differently across anatomical compartments, the background lung may reflect diffuse exposure-driven remodeling, while the peritumoral may capture local tumor-host interactions [14-16]. We conducted a multi-regional modeling strategy, where radiomic features were extracted from multiple anatomical compartments: peritumoral rings (5-, 10-, 15-mm tumor expansions), non-tumor lung parenchyma, and whole-lung regions. For each compartment, we train region-specific classifiers with cross-validated feature selection and integrate predictions via multi-regional fusion. We evaluate generalizability on the external National Lung Screening Trial (NLST) dataset [17]. Beyond predictive performance, we emphasize interpretability through ablation analyses quantifying multi-regional fusion value, smoking-stratified subgroup analyses and feature importance visualization providing clinical context for pollutant-linked CT signatures. Overall, this pathology-anchored

framework demonstrates the utility of multi-regional radiomics for capturing exposure-related features, laying groundwork for scalable CT-based pollutant burden assessment in screening populations.

2 Material and Method

2.1 Dataset

We conducted a retrospective study to develop a CT-based surrogate of pollutant burden in lung adenocarcinoma. The in-house cohort (n=145) comprised patients with paired preoperative chest CT and surgical pathology from routine clinical care. The reference standard was a pathology-derived LPI quantifying anthracotic carbon pigment deposition. LPI was computed from digitized pathology images using an automated computational pathology pipeline, yielding a continuous score. For classification, we dichotomized LPI in the in-house cohort using a quantile-based threshold at q=0.60 (i.e., the 60th percentile), which provides a pragmatic 40/60 split to ensure sufficient representation of the high-LPI subgroup for stable cross-validation while avoiding extreme tail cut points. This quantile threshold corresponded to an LPI value of approximately 0.001 in the in-house cohort, resulting in LPI-high (n=57) and LPI-low (n=88). For external validation, we used a public screening cohort from the NLST [17], accessed through the NCI Imaging Data Commons [18]. We screened NLST cases with expert manual segmentations and available pathology slides meeting our preprocessing requirements, yielding a final external validation set of n=194. We then applied the same computational pathology pipeline to derive LPI scores. To maintain a consistent operational definition of "LPI-high" across cohorts, we applied the same numeric cutoff (LPI = 0.001) derived from the in-house threshold to the NLST cohort, yielding High-LPI n=146 and Low-LPI n=48.

2.2 Feature extraction

The overall framework is shown in **Fig. 1**, We constructed a region-wise radiomic feature library from preoperative chest CT combining standardized preprocessing, anatomically defined regions of interest R_i (ROIs), and multi-family feature extraction.

Anatomical ROI Definition. From radiologist-provided tumor and lung segmentation M_i, we derived: (1) whole lung (R_{Whole}=M_{Lung}); (2) tumor (R_{Tumor}=M_{tumor}); (3) normal lung(R_{Normal}=M_{Lung} - M_{Tumor}); and (4) peritumoral rings (R_{Ring5}, R_{Ring10}, R_{Ring15}) generated by isotropic dilation of tumor mask by radius $r \in \{5, 10, 15\}$mm, computed as $R_{Ring\_r} = [\text{Dilate}(M_{Tumor}, r) - M_{Tumor}] \cap M_{Lung}$, where Dilate$(\cdot)$ denotes morphological dilation with a spherical structuring element of radius r, and the intersection with M_{Lung} restricts the ring to intrapulmonary tissue. All features were computed independently in per region to preserve compartment-specific signatures.

Feature Computation. For each ROI R_i, we extracted comprehensive radiomic features using standardized PyRadiomics configuration [13]. The feature extraction comprised three main categories: (1) First-order statistics quantified the distribution of

voxel intensities $\{x_1, x_2, \cdots, x_N\}$ within each ROI, including mean, variance, skewness, kurtosis, and entropy. (2) Texture features captured spatial patterns through five matrix families: Gray Level Co-occurrence Matrix (GLCM), Gray Level Run Length Matrix (GLRLM), Gray Level Size Zone Matrix (GLSZM), Gray Level Dependence Matrix (GLDM), and Neighborhood Gray Tone Difference Matrix (NGTDM). For instance, GLCM features were computed from the normalized co-occurrence matrix $P(i, j|\delta, \theta)$ representing the joint probability of gray levels i and j at distance δ and angle θ. (3) 3D shape features were computed exclusively for R_{tumor}, as shape features are not well-defined for non-contiguous parenchymal or ring regions. In addition, to capture multi-scale textural phenotypes, we further computed radiomics on filtered representations of the CT image using two complementary approaches: (1) Laplacian-of-Gaussian (LoG) responses at multiple spatial scales σ∈ {1, 2, 3} mm and (2) a 3D stationary Haar wavelet transform, from which a stable subset of sub-bands ($LLL/LLH/LHL/HLL$) was used for feature extraction. These filtered-feature families were designed to emphasize complementary spatial frequency components beyond the native CT appearance. In addition to radiomics, habitat features [19] computed by ROI-cropping and within-case clustering (k = 4), from which we derived habitat volume fractions, habitat-wise mean/variance of HU, and an entropy-based heterogeneity index. The same preprocessing and feature extraction pipeline was applied to the external NLST cohort to ensure that validation reflects true domain shift.

2.3 Region-Specific Learning and Multi-Regional Fusion

As shown in **Fig. 1**, we adopted a two-stage framework under a 5-fold patient-level outer cross-validation protocol: (1) region-specific model training with cross-validated feature selection, and (2) multi-regional fusion predictions *via* multiple ensemble strategies.

Region-Specific Model Training. For each region R_i,. Within each outer fold, feature selection was performed only on the outer-training split *via* stability selection: 40 rounds of random patient subsampling (75%), retaining features selected in ≥60% of rounds. We then evaluated multiple classifiers (Linear SVM, Random Forest, Extra Trees, Gradient Boosting, HistGradientBoosting, XGBoost, CatBoost, and MLP) [20-25] with hyperparameter tuning tuned by nested 3-fold CV within the outer-training split . Performance was measured using patient-level AUC, this yielded out-of-fold predictions $p_K^{(i)}$ per patient i for each region K.

Multi-Regional Fusion. We evaluated six fusion strategies to integrate region-specific predictions: (1) weighted average: $p_w^{(i)} = \sum_{k=1}^{K} w_k p_k^{(i)}$; (2) arithmetic mean: $p_{mean}^{(i)} = \frac{1}{K}\sum_{k=1}^{K} p_k^{(i)}$ (3) logit-space mean: $p_{logit}^{(i)} = \sigma\left(\frac{1}{K}\sum_{k=1}^{K} z_k^{(i)}\right)$ where $z_k^{(i)} = \log\left(p_k^{(i)}/(1-p_k^{(i)})\right)$ and $\sigma(z) = 1/(1+e^z)$; and (4-6) stacking meta-learners (Logistic Elastic Net, Logistic L2, SVM-RBF) trained on meta-features $F_{meta}^{(i)} = \left[z_1^{(i)} \cdots z_K^{(i)}, \bar{z}^{(i)}, \sigma_z^{(i)}\right]$, where $\bar{z}^{(i)}$ and $\sigma_z^{(i)}$ are the mean and standard deviation of region-specific logits. Meta-learner hyperparameters tuned by nested 3-fold CV within the outer-training split. We performed exhaustive grid search across all region-classifier

combinations and fusion strategies. Optimal configuration was selected by highest out-of-fold performance across all region-classifier combinations and fusion methods.

3 Experiments and Results

Model performance was evaluated at the patient level using out-of-fold predictions to prevent information leakage. Uncertainty was estimated via non-parametric bootstrap resampling (B = 2000) with 95% confidence intervals from empirical percentile distributions.

3.1 Main performance

Fig. 2 summarizes the main performance of our CT-LPI prediction framework on the in-house cohort and the external NLST cohort. In the in-house cohort, the model achieved strong discrimination with a ROC-AUC of 0.733 (95% CI: 0.644–0.812) and an average precision (AP) of 0.636 (95% CI: 0.538-0.743), indicating reliable separation between the two LPI strata and meaningful precision across the recall range. On the external NLST cohort, performance remained above chance with a ROC-AUC of 0.609 (95% CI: 0.513-0.702), supporting generalizability under domain shift. Notably, AP increased to 0.808 (95% CI: 0.755-0.869). The higher AP in NLST is consistent with AP being sensitive to class distribution, given the larger proportion of high-LPI labels in NLST. Overall, the concordant ROC and PR results demonstrate that the model captures pollutant-burden–associated imaging signatures and transfers to an independent public dataset.

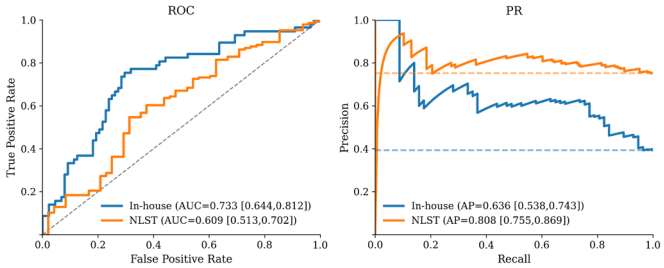

Fig. 2. Model performance on in-house and NLST dataset. (A) Receiver operating characteristic (ROC) curves showing discrimination performance on the in-house cohort (AUC=0.733, 95% CI: 0.644–0.812) and external NLST cohort (AUC=0.609, 95% CI: 0.513–0.702). (B) Precision-recall (PR) curves demonstrating average precision of 0.636 (95% CI: 0.538–0.743) for in-house validation and 0.808 (95% CI: 0.755–0.869) for external validation.

3.2 Multi-regional evidence

To test whether pollutant-associated features are confined to a single anatomical compartment or distributed across complementary lung compartments, we compared

region-specific models against multi-region fusion and performed targeted regional contribution analyses (**Fig. 3**).

Single-region vs. fusion performance (Fig. 3A). The best single-region model achieved AUCs ranging from 0.578 to 0.648, with the whole-lung model providing the strongest individual signal (AUC = 0.648), followed by Ring5 (AUC = 0.617) and normal lung parenchyma (AUC = 0.590). In contrast, multi-region fusion consistently improved discrimination, with the best results obtained by a fixed weighted average that emphasized normal lung parenchyma and whole lung (weights: Normal lung: 0.40, Whole lung: 0.20, Ring10: 0.15, Tumor: 0.15, Ring5: 0.05, Ring15: 0.05) reaching AUC = 0.733, outperforming simple averaging (mean: 0.707; logit-mean: 0.705) and stacking-based meta-learners (stack-EN: 0.667; stack-LR: 0.659; stack-SVM: 0.560). These results indicate that complementary information is present across compartments and that a late-fusion strategy can more effectively aggregate region-specific signals than any single ROI alone.

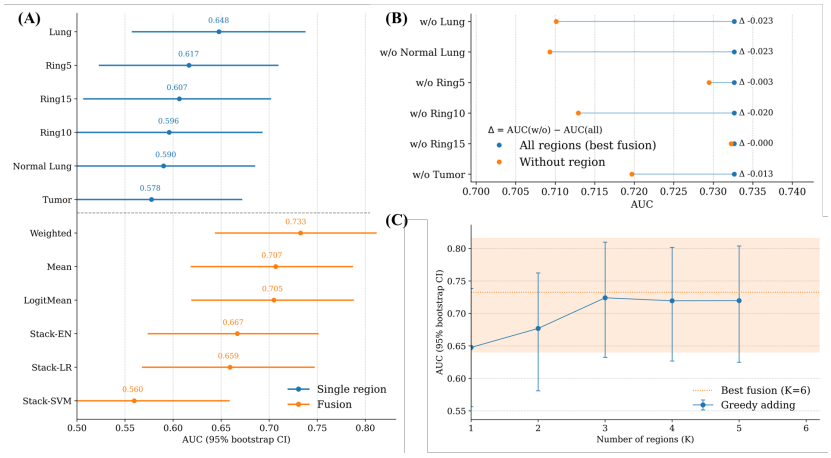

Fig. 3. Single- vs. multi-region fusion performance and regional contributions. (A) AUC of the best single-region models (blue) and fusion strategies (orange); points denote AUC with 95% bootstrap CIs. (B) Leave-one-region-out ablation of the best fusion: all-regions AUC (blue) vs. removing one region (orange); ΔAUC indicates the change after exclusion. (C) Greedy forward adding: AUC versus number of included regions; dashed line marks the full-fusion AUC.

Regional contribution analyses (Fig. 3B–C). Leave-one-region-out ablation on the best fusion model (Fig. 3B) showed that excluding whole lung or normal lung led to the largest performance drops (both ΔAUC = -0.023), followed by Ring10 (ΔAUC = -0.020) and tumor (ΔAUC = -0.013), whereas removing Ring5 had a minimal effect (ΔAUC = -0.003) and Ring15 contributed negligibly in this cohort (ΔAUC ≈ 0). Consistently, the greedy forward-adding curve (Fig. 3C) demonstrated rapid gains when moving from one to a few regions (from AUC = 0.664 at $K = 1$ to ~0.724 at $K = 3$), followed by diminishing returns as additional regions were included, with the full fusion (all regions) achieving the highest AUC (0.733) within its bootstrap CI band.

Together, these findings support the multi-regional hypothesis: CT-LPI related phenotypes are not localized to a single compartment but are instead captured across lung-wide parenchymal patterns and peritumoral context, and fusing these complementary signatures yields improved and more robust performance.

3.3 Subgroup analysis

We conducted smoking-stratified analyses to assess whether CT-LPI prediction could be confounded by smoking status. In our cohort, smoking composition varied across LPI strata: in the Low-LPI group, 51 (58%) were smokers and 37 (42%) were never-smokers; in the High-LPI group, 38 (67%) were smokers and 19 (33%) were never-smokers, motivating subgroup evaluation. ROC analyses stratified by smoking status showed comparable discrimination between never-smokers (AUC = 0.688) and smokers (AUC = 0.754), with a numerically notable but statistically non-significant difference (ΔAUC = 0.065; $p = 0.490$). It suggests that High/Low LPI groups may exhibit more distinguishable imaging features in the presence of smoking-related parenchymal changes. Importantly, both subgroups demonstrated clinically meaningful discrimination (AUC > 0.68), indicating that CT-based LPI prediction captures pollution exposure signals independent of smoking status and is not solely driven by smoking history.

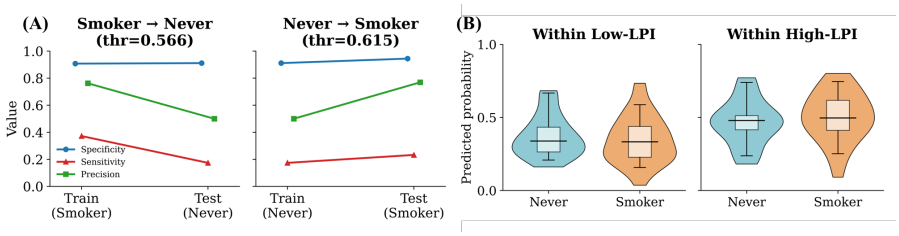

Fig. 4. Smoking-subgroup analyses to assess potential confounding by smoking status in LPI classification. (A) threshold transfer at fixed high specificity reveals to evaluate operating-point shift (B) within-label score distributions show no significant subgroup-dependent score shift.

To probe potential operating-point bias, we evaluated operating-point stability by transferring a probability threshold chosen to achieve high specificity (Spec≥0.90) in one smoking subgroup to the other (**Fig.4A**). The transferred threshold preserved high specificity in the target subgroup (both directions maintained Spec > 0.85), indicating no marked subgroup-dependent inflation of false positives. Moderate shifts in sensitivity and precision reflect expected consequences of differing label prevalence (High-LPI: 67% in smokers vs. 42% in never-smokers) rather than smoking-driven bias. Finally, within-label score distributions (Low-LPI and High-LPI separately) showed no significant smoking-dependent score shift (**Fig. 4B**). Collectively, these results support that the model primarily captures LPI-related imaging signal instead of functioning as a proxy smoking classifier.

3.4 Interpretability Analysis

To interpret the decision process, we performed a region-wise feature importance analysis on the best performing single-region classifiers and summarized the top-5 most influential radiomic features per region (**Fig. 5**). To connect regional interpretability to the final ensemble behavior, each region panel is annotated with its fusion weight (w) from the best fusion strategy, highlighting how strongly that region contributes to the overall prediction. In addition, bar colors encode the direction of association with LPI-high vs. LPI-low, allowing simultaneous inspection of both impact and directionality.

Overall, the interpretability results show that parenchymal (normal lung) radiomics dominates the ensemble (Normal Lung, $w = 0.40$), with texture heterogeneity features such as GLCM-SumSquares and GLDM-Dependence Variance/Entropy emerging as the most influential, suggesting that pollutant burden is reflected in global changes of lung texture beyond the tumor region. Whole-lung features ($w = 0.20$) similarly emphasize texture statistics (e.g., GLCM-ClusterShade, GLSZM-ZonePercentage) and distributional descriptors (e.g., first-order entropy), reinforcing a global parenchymal signal. In parallel, the model also leverages tumor ($w = 0.15$) and peritumoral ring information (Ring10, $w = 0.15$; Ring5/Ring15, $w = 0.05$ each): the tumor region highlights intensity-tail and heterogeneity markers (e.g., first-order 10th percentile, kurtosis, GLRLM-RunPercentage, GLSZM-LAIGLE), while ring regions are characterized by complementary texture/habitat-related descriptors (e.g., GLSZM gray-level variance, NGTDM contrast, and habitat-like features), consistent with pollutant-associated remodeling that extends into the peritumoral microenvironment. Taken together, these findings indicate that the ensemble's discrimination of LPI status is primarily driven by texture and heterogeneity patterns across normal lung and whole-lung parenchyma, with tumor/peritumoral features providing supportive, localized complementary cues

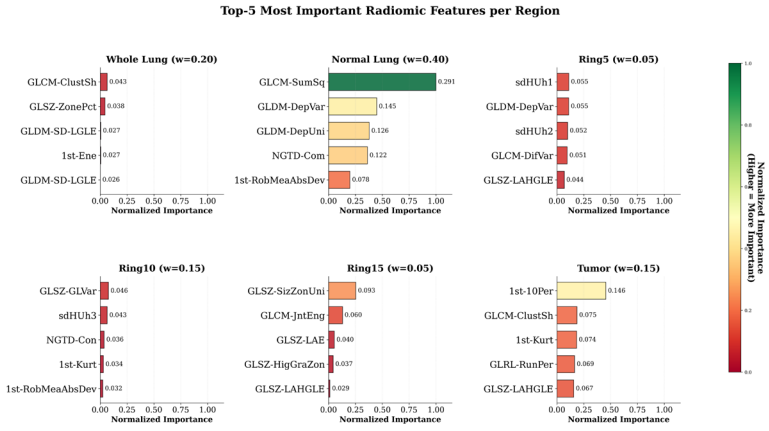

Fig. 5. Top radiomic features per region with permutation importance. Top-5 radiomic features from the best single-region classifiers for each ROI. Panel headers report each region's fusion weight (w) in the final weighted-average ensemble. Bar color encodes direction. Abbreviations: GLCM = gray-level co-occurrence matrix; GLDM = gray-level dependence matrix; GLSZM = gray-level size zone matrix; NGTDM = neighborhood gray-tone difference matrix.

4 Discussion and Conclusion

We developed a CT-based surrogate for tissue-level pollutant burden using pathology-anchored multi-regional radiomics in lung adenocarcinoma. Multi-regional fusion (AUC=0.733) substantially outperformed single-region models (best AUC=0.664), with normal lung parenchyma contributing most strongly (w=0.40). Texture heterogeneity features dominated, suggesting chronic particulate exposure induces measurable architectural changes detectable by CT. Smoking-stratified analyses showed similar performance between never-smokers and smokers, indicating the model captures pollution-specific signals rather than smoking effects. A key limitation is that our current cohort comprises surgical cancer patients, as pathology-derived LPI requires tissue specimens. Future work should extend CT-LPI to nodule cohorts and screening populations, potentially using surrogate labels from exposure history or longitudinal imaging patterns (i.e., consistent temporal changes in nodule-associated phenotypes). External validation on NLST demonstrates initial generalizability. This work establishes proof-of-concept for non-invasive exposure biomarkers.

Acknowledgments. This work and/or data generated is supported by the Spatial Ecology & QUantitative pathOlogy Image Analytical platform (SEQUOIA) through the MD Anderson STrategic Research Initiative Development (STRIDE) Program and the Institute for Data Science in Oncology (IDSO) at The University of Texas MD Anderson Cancer Center. Additional support was provided by LungSPORE grant P50 CA070907 from the NIH and the MD Anderson Translational Molecular Pathology-Immunoprofiling Lab (TMP-IL) Platform; and the Cancer Prevention and Research Institute of Texas (CPRIT) RP260222.

Disclosure of Interests. The authors have no competing interests to declare that are relevant to the content of this article.

References

1. Sung, H., et al., Global cancer statistics 2020: GLOBOCAN estimates of incidence and mortality worldwide for 36 cancers in 185 countries. CA: a cancer journal for clinicians, 2021. **71**(3): p. 209-249.
2. Schabath, M.B. and M.L. Cote, Cancer progress and priorities: lung cancer. Cancer epidemiology, biomarkers & prevention, 2019. **28**(10): p. 1563-1579.
3. Burt, J.R., et al., Non-small cell lung cancer in ever-smokers vs never-smokers. BMC medicine, 2025. **23**(1): p. 3.
4. Jani, C.T., et al., Evolving trends in lung cancer risk factors in the ten most populous countries: an analysis of data from the 2019 Global Burden of Disease Study. EClinicalMedicine, 2025. **79**.
5. Turner, M.C., et al., Long-term ambient fine particulate matter air pollution and lung cancer in a large cohort of never-smokers. American journal of respiratory and critical care medicine, 2011. **184**(12): p. 1374-1381.
6. Bhamani, A., et al., Low-dose CT for lung cancer screening in a high-risk population (SUMMIT): a prospective, longitudinal cohort study. The Lancet Oncology, 2025. **26**(5): p. 609-619.

7. Kim, W.-D., Phenotype of Chronic Obstructive Pulmonary Disease Based on Computed Tomography–Defined Underlying Pathology. Tuberculosis and Respiratory Diseases, 2022. **85**(4): p. 302.
8. Ardakani, A.A., et al., Interpretation of radiomics features–a pictorial review. Computer methods and programs in biomedicine, 2022. **215**: p. 106609.
9. Li, C., et al., Application of deep learning radiomics in oral squamous cell carcinoma–Extracting more information from medical images using advanced feature analysis. Journal of Stomatology, Oral and Maxillofacial Surgery, 2024. **125**(3): p. 101840.
10. Amudala Puchakayala, P.R., et al., Radiomics for improved detection of chronic obstructive pulmonary disease in low-dose and standard-dose chest CT scans. Radiology, 2023. **307**(5): p. e222998.
11. Zhu, Z., et al., Development and application of a deep learning-based comprehensive early diagnostic model for chronic obstructive pulmonary disease. Respiratory Research, 2024. **25**(1): p. 167.
12. Wang, M., et al., Association between long-term exposure to ambient air pollution and change in quantitatively assessed emphysema and lung function. Jama, 2019. **322**(6): p. 546-556.
13. Namdar, K., et al., Open-radiomics: a collection of standardized datasets and a technical protocol for reproducible radiomics machine learning pipelines. BMC Medical Imaging, 2025. **25**(1): p. 312.
14. Jha, A.K., et al., Radiomics: a quantitative imaging biomarker in precision oncology. Nuclear Medicine Communications, 2022. **43**(5): p. 483-493.
15. Eckhardt, C.M. and H. Wu, Environmental exposures and lung aging: molecular mechanisms and implications for improving respiratory health. Current environmental health reports, 2021. **8**(4): p. 281-293.
16. Zhang, S., et al., The peritumor microenvironment: physics and immunity. Trends in cancer, 2023. **9**(8): p. 609-623.
17. Team, N.L.S.T.R., The national lung screening trial: overview and study design. Radiology, 2011. **258**(1): p. 243-253.
18. Thiriveedhi, V., et al., TotalSegmentator segmentations and radiomics features for NCI Imaging Data Commons CT images. Zenodo https://doi. org/10.5281/zenodo, 2024. **8347012**.
19. Shang, Y., et al., Habitat imaging with tumoral and peritumoral radiomics for prediction of lung adenocarcinoma invasiveness on preoperative chest CT: a multicenter study. American Journal of Roentgenology, 2024. **223**(4): p. e2431675.
20. Valkenborg, D., et al., Support vector machines. American journal of orthodontics and dentofacial orthopedics, 2023. **164**(5): p. 754-757.
21. Salman, H.A., A. Kalakech, and A. Steiti, Random forest algorithm overview. Babylonian Journal of Machine Learning, 2024. **2024**: p. 69-79.
22. Sharma, D., R. Kumar, and A. Jain, Breast cancer prediction based on neural networks and extra tree classifier using feature ensemble learning. Measurement: Sensors, 2022. **24**: p. 100560.
23. Ali, Z.A., et al., eXtreme gradient boosting algorithm with machine learning: A review. Academic Journal of Nawroz University, 2023. **12**(2): p. 320-334.
24. Mert, İ., Prediction of Wind Speed Using Tree-Based Ensemble Algorithms: CatBoost, HistGBM, and XGBoost. International Journal of Multidisciplinary Studies and Innovative Technologies, 2025. **9**(1): p. 145-150.
25. Ostovar, A., D.D. Davari, and M. Dzikuć, Determinants of design with multilayer perceptron neural networks: A comparison with logistic regression. Sustainability, 2025. **17**(6): p. 2611.